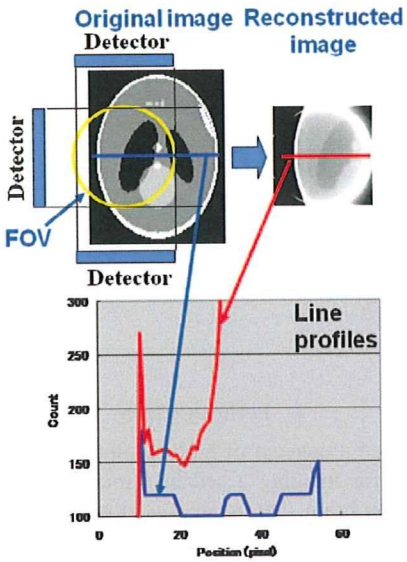

Fig. 1. The artifact and overestimation on the reconstructed image due to truncation.

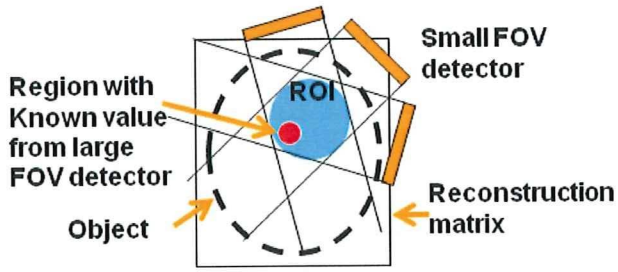

Fig. 2. Schematic diagram showing the solution of the interior problem.

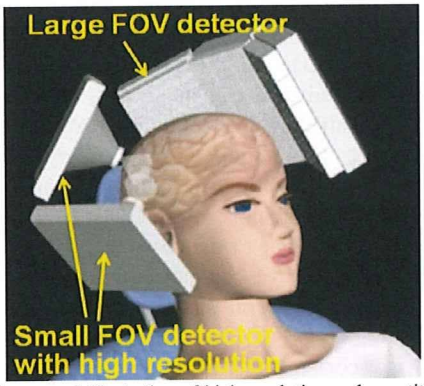

Fig. 3. Conceptual illustration of high resolution and quantitative SPECT system for imaging a selected small ROI of human brain.

III. Preliminary Experiment

For proof of our concept, we performed preliminary experiment using pinhole SPECT and Hoffman brain phantom [3]. The reconstruction ROI contained the region outside the brain, that is, almost zero count as the priori knowledge [4]. The truncated data were reconstructed by truncation compensated 3D-OSEM (TC-3DOSEM) reconstruction method for pinhole SPECT [5].

Figure 4 shows the experimental setup. We scanned a part of Hoffman brain phantom using the rotating stage and 1-mm pinhole collimator fitted to clinical SPECT gamma camera (GCA7200A, Toshiba, Japan). As for the scan parameters, the phantom was filled with Tc-99m of 1,480 MBq and scanned for 2 hours, the radius of rotation was 95mm, the imaging FOV was 95 mm, and the rotation angle was 180 degrees. This radius of rotation is that collimator doesn't hit again the phantom in case of circular orbit and 180 degrees rotation. And also, we scanned same phantom using parallel collimator to compare in terms of spatial resolution.

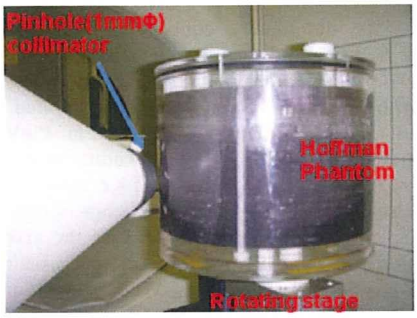

Fig. 4. Experimental setup for scanning Hoffman brain phantom by pinhole SPECT.

Figure 5 shows results of human brain phantom study. In case of clinical SPECT with parallel collimator, the resolution of the reconstructed image was low. In case of pinhole collimator and conventional 3DOSEM, the resolution was high, but the artifact appeared at the edge of ROI and the voxel counts were overestimated. On the other hand, combination of pinhole collimator and TC-3DOSEM provide high resolution image and eliminated the artifact and the overestimation. In this experimental geometry using pinhole collimator, theoretical resolution was approximately 2 mm.

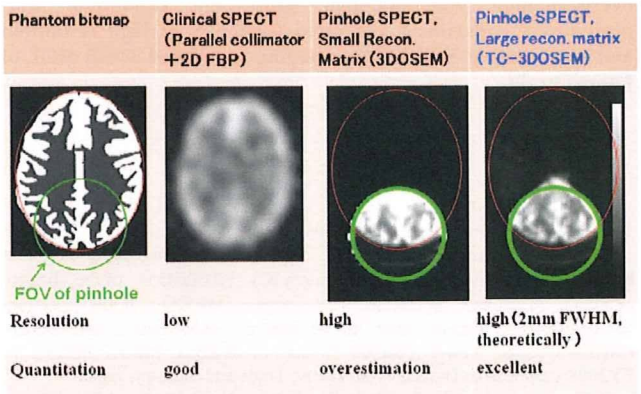

Fig. 5. Comparison of the reconstructed image from preliminary experiment using brain phantom.

IV. Conclusion

We have designed the concept of high resolution and quantitative SPECT for imaging a selected small ROI of human brain. And also, the preliminary experiment suggested

feasibility of high resolution and quantitative SPECT for human brain.

REFERENCES

[1] H. Kudo, M. Courdurier, F. Noo, and M. Defrise, "Tiny a prior knowledge solves the interior problem in computed tomography," *Phys. Med. Biol.*, vol. 53, no. 9, pp. 2207-2231, 2008.

[2] R. Pani, R. Pellegrini, M. N. Cinti, P. Bennati, M. Betti *et al.*, "$LaBr_3$:Ce crystal: The latest advance for scintillation cameras," *Nucl Instrum Meth A.*, vol. 572, pp. 268-269, 2007.

[3] E. J. Hoffman, P. D. Cutler, W. M. Digby, and J. C. Mazziotta, "3D phantom to simulate cerebral blood flow and metabolic images for PET," *IEEE Trans. Nucl. Sci.*, vol. 37, pp. 616-620, 1990.

[4] M. Defrise, F. Noo, R. Clackdoyle, and H. Kudo, "Truncated Hilbert transform and image reconstruction from limited tomographic data," *Inverse Problems*, vol. 22, pp. 1037-1053, 2006.

[5] T. Zeniya, H. Watabe, A. Sohlberg, T. Inomata, H. Kudo, et al., "3D-OSEM reconstruction from truncated data in pinhole SPECT," *2007 IEEE Nuclear Science Symposium Conference Record*, vol. 6, pp. 4205-4207, 2007.

Performance estimation of high resolution SPECT for the human brain by Monte Carlo simulation of scintillation lights

Y. Hirano, T. Zeniya, H. Watabe, *Member, IEEE* and H. Iida, *Member, IEEE*

***Abstract*–We developed the high resolution SPECT for the human brain. The SPECT has two kinds of detectors. One middle-size detector views whole a head. The other small detector which has extremely resolution (~1mm) views localized region. These detectors are rotated simultaneously. The large detector consists of NaI(Tl) scintillator (15cm×20cm), 15 flat panel type multi-anode PMTs (H8500 Hamamatsu). The performance evaluation, spatial and energy resolution, has performed. The obtained spatial resolutions of X-direction and Y-direction are 2.4mm and 2.1mm(FWHM), respectively, and 10%@140keV (FWHM) of the energy resolution was obtained. On the other hand, the small detector for the regional field of view is under the development. We will use the $LaBr_3$(Ce) as the scintillator which has large amount of scintillation lights lather than that of NaI(Tl). The performance of $LaBr_3$(Ce) has estimated by the Monte Carlo simulation of scintillation lights after the comparing the result of the experiments of the middle-size detector with that of the simulation. In this simulation, many optical properties of materials are considered. Using this simulation, the influence of the scintillator thickness on the spatial resolution has investigated. Also, main contribution is given to spatial resolution has been investigated by changing some optical properties such as the amount of emission lights, the refractive index of optical coupling grease and the index of reflector in this simulations. The small detector will be used with a pin-hole collimator, therefore gamma-rays obliquely enter the detector. The spatial resolutions of oblique and parallel incident are also compared.**

I. Introduction

We have been developed a high resolution Single Photon Emission Computed Tomography (SPECT) for the human brain aiming at clinical inspections. This SPECT has two kinds of detectors and rotated simultaneously. One is a middle -size detector, the other is a small size detector. The middle-size detector views whole human brain with parallel collimator. The small detector views localized region with pinhole or cone-beam collimators. However, in case of large object like humans brain, the projection data are truncated by radioisotope outside of a small field of view (FOV). Due to the truncation, on the reconstructed image, the artifact appears and the voxel values are overestimated. This hampers quantitative assessment of physiological functions. We have developing the new truncation compensated 3D-OSEM (TC-3DOSEM) reconstruction method. We use a image of the middle-size detector without truncation as initial image, and reconstruct image of the small detector .The truncated data can be successfully reconstructed [1][2]. The conceptual diagram and aspect of the detector are shown in Fig.1. The middle-size detector has been completed, and checked the performance such as the spatial resolution, and the energy resolution. On the other hand, we have plan to use $LaBr_3$(Ce) scintillator as the scintillator of small size detector to improve the resolutions. A higher resolution is expected using $LaBr_3$(Ce) because of large amount of scintillation lights which is about 1.6 times larger than that of NaI. Then, we estimated how much resolution will be obtained using $LaBr_3$(Ce) and investigated the influence of a scintillator thickness on the spatial resolutions. The scintillation lights are simulated with Monte Carlo method. In addition, we investigated what is the main factor of contribution to the spatial resolutions by changing optical properties. In order to make high resolution system, we need previous estimation of performance by using some simulations, and this simulation will be useful to design detector system.

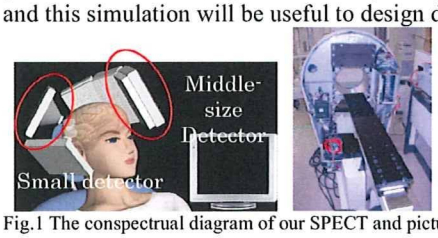

Fig.1 The conspectrual diagram of our SPECT and picture of the detector.

II. Materials and Method

The middle-size detector has been constructed. The detector consist of NaI scintillator (15cm×20cm), 12 flat panel type multianode PMTs (H8500 manufactured by HAMAMATSU, 5cm×5cm) and collimators. The PMT has 64 small anodes (5.2mm×5.2mm) shown in Fig.2(left and center). High resolution has achieved by the Anger method using 768 anodes. After the operation check, the energy resolution and the spatial resolutions are measured as the performance evaluation. In order to estimate resolutions, we put the collimator which has 170 holes(1.5φ) with interval 15mm on the NaI, moreover, put the plane source (Tc-99m :140keV) shown in Fig.2(right). The spatial resolutions are derived by some fitting results of the projection to the X-direction and Y-direction. The fitting functions, which considers the diameter of holes are described fallowing a function,

$$f(x)=\frac{1}{2a}\left\{erf\left(\frac{a+b-x}{2\sigma}\right)-erf\left(\frac{b-x}{2\sigma}\right)\right\},$$

Y.Hirano, T.Zeniya, H.Watabe and H.Iida are with the Department of Investigative Radiology, Advanced Medical Engineering Center, National Cardiovascular Center Research Institute, 5-7-1 Fujishirodai, Suita City, Osaka, 565-8565 Japan (e-mail: hirano@ri.ncvc.go.jp).

9781-4244-3962-1/09/$25.00 ©2009 IEEE

where a, b are shown in Fig.3. σ^2 is the deviation of Gauss function. The spatial resolutions can be obtain by the $2.35\times\sigma$. The energy resolutions of each position also can be obtained by the fitting of exponential and Gauss functions.

Fig.2 NaI scintillator (15cmx25cm)(left). 5x3 H8500 Flat panel type PMT(center). The collimator with 170 holes(right). The diameter is 1.5mm and distributed at 15mm intervals. The thickness is 10mm.

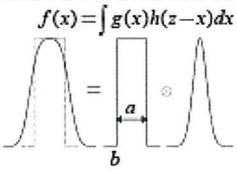

Fig3. Fitting function. $f(x)$ is convolution function of uniform and Gauss function.

The Monte Carlo simulation has performed with the same geometry of middle-size detector, and compared the result of the simulation with that of the experiments. The simulated processes are listed below and shown in Fig.4.

1. Gamma rays enter the scintillator.
2. Scintillation lights are emitted to 4π-derecion and the amount of lights is proportional to the energy deposit.
3. Scintillation lights propagate in some materials such as the scintillator, optical grease, light guide (glass) and PMT window.
4. Optical processes such as reflection, refraction at boundaries and absorption, which have wavelength dependence are considered.
5. When scintillation lights reach an anode of the PMT, detection or not are determined by the quantum efficiency.

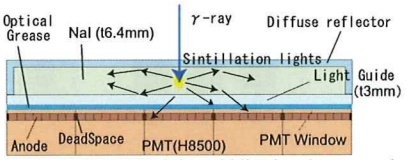

Fig.4 The simulation geometry of the middle-size detector. The scintillation lights are propagated through some materials.

After the comparing the simulation and experiment, we have investigated the influence of a scintillator thickness on the spatial resolution. We will use $LaBr_3(Ce)$ as scintillator of the small detector. The size is 10cm x 10cm, and the thickness is not yet determined. Expected spatial resolutions are estimated by the simulation changing thickness of the scintillator (10mm, 8mm, 6.4mm, 5.8mm, 4mm, 2mm and 1mm). The incident gamma-rays are 15mm apart shown in Fig.5. The difference of optical properties between NaI(Tl) and $LaBr_3(Ce)$ is listed in Tab.1 and shown in Fig.6.

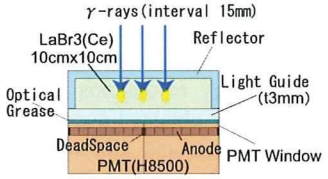

Fig.5 The simulated geometry of the small size detector. The incident parallel gamma-rays are apart from 15mm.

Tab.1 The scintillator properties of NaI(Tl) and $LaBr_3(Ce)$

	Density (g/cm3)	Relative output	Deliquescent	Time Constant	Refractive Index	Peak Wave length[nm]
NaI(Tl)	3.67	1	Strong	230	1.85	425
$LaBr_3(Ce)$	5.3	1.6	Strong	16	1.9	385

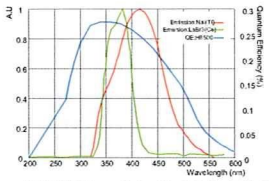

Fig.6 Emission spectra of NaI(Tl) and $LaBr_3(Ce)$ and the quantum efficiency of H8500 PMT

In order to know what optical property is critical of the spatial resolution, some simulations of the small detector changing some properties have performed. The changing parameters are the emission spectra of $LaBr_3(Ce)$→that of NaI(Tl), the amount of scintillation lights of $LaBr_3(Ce)$(68photon/keV)→ that of NaI(Tl)(32photon/keV), the refractive index of $LaBr_3(Ce)$(1.9)→that of NaI(Tl)(1.85), the refractive index of optical grease(1.4)→that of air(1.0), index of reflector 95%→ 90% and light guides thickness 3mm→1mm. Finally, the difference of the spatial resolution between using a pin-hole collimator and using a parallel collimator, in other words, the difference between parallel incident and oblique incident has investigated. The gamma-rays are entered into the scintillator at 49 points with interval 15mm in this simulation shown in Fig.7

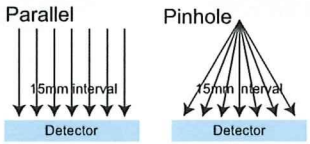

Fig.7 The conceptual diagram of the simulations using pin-hole collimator and using parallel collimator.

III. Result and Discussion

III-1 Performance evaluation of the middle-size detector

The experimental reconstructed position of middle-size detector is shown in Fig.8 using the collimator with 170 hoes, and the projection to the X-direction of 6th lines from the bottom and Y-direction of 8th columns from the left are also shown in Fig.9. The spatial resolutions at 170 points (at the points of the collmator hole) for X-direction and Y-direction are derived by fitting of each projection (10 projections to the X-direction and 17 projections to the Y-direction). The re-

sults of the spatial resolutions are shown in Fig.10. Also, the energy spectrum at the center of the detector is shown in Fig.11(left), and the energy resolutions at 170 points are shown in Fig.11(right). The obtained averages of the spatial resolutions are 2.43±0.27mm and 2.08±0.18mm (FWHM), and the best values are 2.2mm and 1.7mm for X-direction and Y-direction, respectively. These averages are derived by the spatial resolutions excluding resolution of edges. We can see the tendency that the center of the detector is better spatial resolution lather than that of the edges. Because of the small number of resistor used in Anger method, the spatial resolutions of Y-direction with less number of the resistors have better than that of X-direction. On the other hands, we can't see the position dependence of the energy resolutions. The average energy resolution is 10.28±0.17% (FWHM).

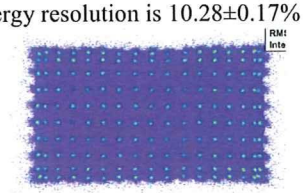

Fig.8 The experimental result of reconstructed position of the middle-size detector by Anger method.

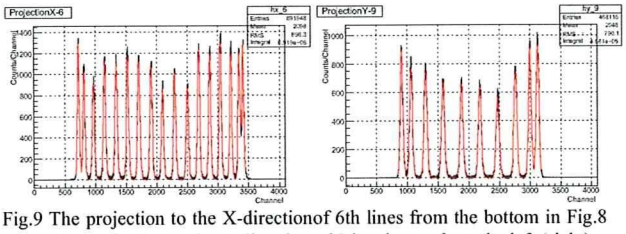

Fig.9 The projection to the X-directionof 6th lines from the bottom in Fig.8 (left). The projection to the Y-direction of 8th columns from the left (right)

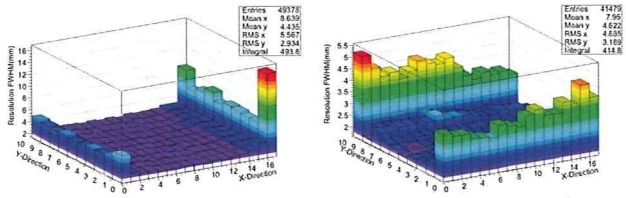

Fig.10 The spatial resolutions at 170 points. The left (right) figure shows the spatial resolution of X (Y) direction.

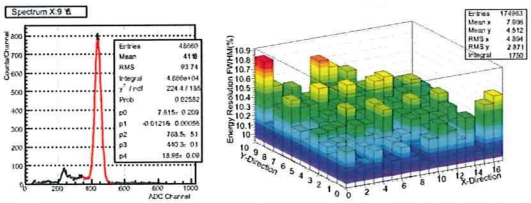

Fig.11 The energy spectrum at the almost center of the detector (left). The energy resolution at 170 points (right)

III-2 Comparison between experiment and simulation

The simulation result of the reconstructed position of middle-size detector is shown in Fig.12 (left), and the projections are shown in Fig.13(right). Also, the comparisons of the spatial and energy resolutions are listed in Tab.2. The good agreement of the projection is obtained. However, the resolutions of simulation overestimate that of the experiment. In order to correspond to the result of experiment, we give fluctuation such as electrical noise.

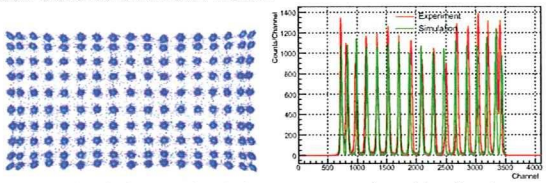

Fig.12 The simulation result of the reconstructed position by Anger method(left).The comparison of the projections(right) between the experiment(red lins) and the simulation(green line).

Tab.2 The comparison of the energy and spatial resolutions.

FWHM	Spatial Resolution X	Spatial Resolution Y	Energy Resolution
Simulation	1.71 mm	1.54 mm	7.1 %
Experiment	2.43 mm	2.08 mm	10.3 %

III-3 Influence of scintillator thickness on spatial resolution

Using the geometry of the small detector, influence of the scintillator thickness on the spatial resolution and the detection efficiency has investigated, and the results are listed in Tab.3 together with the result of NaI(Tl) of thickness 6.4mm. The thickness 6.4mm is same as the middle-size detector. The thickness 5.8mm of $LaBr_3(Ce)$ has same stopping power as that of t6.4mm NaI(Tl). The reconstructed positions and the projections are also shown in Fig.13 together with distribution of photo-electrons on the PMT anodes. The thinner scintillator, the better spatial resolutions are obtained because the emission point of the scintillation lights is close to the PMT anodes, which suppress the spread of distribution of scintillation lights shown in Fig.13(upper). However, the detection efficiency degreases. Therefore, we must decide a scintillator thickness considering both efficiency and spatial resolutions.

Tab.3 The spatial resolutions and efficiency of each thickness

Thickness	t10mm	t8mm	t6.4mm	t6.4mmNaI(Tl)	t5.8mm	t4mm	t2mm	t1mm
Spatial Resolution (mm)	2.2	1.9	1.8	2.0	1.7	1.4	1.0	0.8
Efficiency (%)	90	85	76	74	74	60	37	19

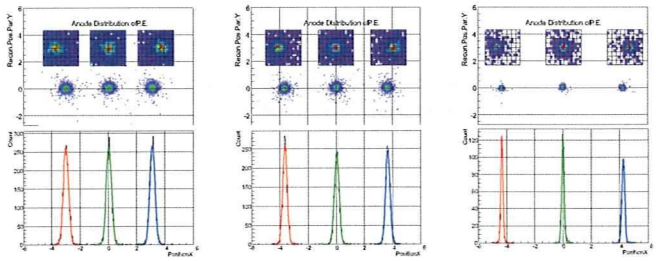

Fig.13 The result of distribution of reconstructed position and projections for each thickness (t10mm, t5.8mm and t1mm from the left), together with the distribution of photo-electrons on the PMT anodes.

III-4 Influence of other optical properties on spatial resolution

Some optical properties are changed described in II in the simulation of the small detector. The results of each case are listed in Tab.4. Also, the distribution of absorbed scintillation light has simulated. The percentages of total absorbed photons for each material are also listed in Tab.4. We can see the re-

duction of the spatial resolution in two cases. One is the refractive index of the optical grease is replaced with that of air. The other is decrease of amount of scintillation light by about half. Other changes of the property have small contribution to the spatial resolution.

Tab.4 Spatial and energy resolutions changing some optical properties and the distribution of the absorbed photons.

Resolution or Absorber name	LaBr3:Emission → NaI:Emission	LaBr3:yield → NaI:yield	LaBr3:Index → NaI:Index	Grease:Index → Air:Index	Reflecto n 95% → Reflecto n 90%	LightGuide:3m → LightGuide:1mm	LaBr3:15.8mm (Criterion)
Spatial Resolution (mm)	1.7	2.1	1.7	2.5	1.7	1.7	1.7
Energy Resolution FWHM(%)	6.1	7.7	5.9	6.4	6.3	5.8	5.9
Abs. by Scintillator (%)	1.6	1.9	1.6	2.5	1.7	1.6	1.7
Abs. by PMT(detect) (%)	20	19	20	18	17	19	18
Abs. by PMT(miss) (%)	56	53	56	49	47	55	55
Abs. by PMT Dead Space(%)	14	13	14	10	12	16	14
Abs. by Reflector (%)	8	11	8	19	19	8	9
Abs. by Other (%)	0.4	2.1	0.4	1.5	3.3	0.4	2.3

Finally, the distributions of reconstructed positions are shown in Fig.14 for the parallel incident and the oblique incident. The obtained averages of spatial resolutions are 1.48mm and 1.68mm for parallel incident and oblique incident, respectively. The spatial resolutions of the oblique incident (using pin-hole collimator) has worse resolutions lather than that of parallel incident because of spread of interaction points on the horizontal surface.

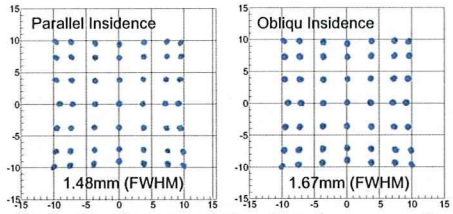

Fig.14 The distribution of reconstructed positions by Anger method. The left (right) figure is result of parallel (oblique) incident.

This study will be useful for the design the both new and better detectors. However, a good agreement between the simulation and the experiments has not obtained for the absolute values of the spatial and energy resolutions. As the future task, we will enhance the accuracy of the simulation by eliminating the uncertainty of optical parameters and specifying other parameters which are not considered in this simulation.

REFERENCES

[1] T.Zeniya, *et al.* IEEE 2008 Nuclear Science Symposium Conference Record. pp. 5229-5231
[2] T.Zeniya, *et al.* IEEE 2009 Medical Imaging Conference (oral presentation)
[3] http://geant4.web.cern.ch/geant4/

Interior SPECT Reconstruction Problem with Tiny *a proiri* Knowledge – An Application for High Resolution Pinhole Brain Imaging

Qiu Huang, Tsutomu Zeniya, Hiroyuki Kudo, Hidehiro Iida, and Grant T. Gullberg

Abstract— **The quantitation of cerebral blood flow (CBF) and cerebral vascular reactivity (CVR) are valuable in diagnosing brain ischemia, and the quantitation of benzodiazepine receptor density is important in evaluating neuronal damage due to ischemic effects. To better evaluate cerebral autoregulation, a high resolution brain single photon emission computed tomography (SPECT) imager is being built that provides an image of the entire brain for support information in the reconstruction of the interior problem from small field-of-view, truncated projections for high resolution ROI imaging.**

Kudo *et al.* presented a unique and stable solution to the interior problem in computed tomography (CT) given tiny *a proiri* knowledge of the object. In this work we advance their result to the interior reconstruction problem in SPECT where a uniform attenuation map is assumed in brain imaging.

In the theory, differentiation followed by backprojection (DBP) of truncated SPECT data is shown to obtain the truncated weighted Hilbert transform. Then with *a proiri* information on a small part of the region-of-interest (ROI), the other part of the ROI is shown to be available using the projection onto convex sets (PCOS) method. Simulations show that the algorithm provides quantitative results for the reconstruction of the fan-beam tomographic data. Iterative reconstruction of the pinhole data is under investigation to verify the accuracy of the central slice and to provide reasonable results for regions off the central slice.

Index Terms—**interior problem, SPECT, uniform attenuation, brain imaging.**

I. Introduction

The Department of Investigative Radiology at the National Cardiovascular Center Research Institute in Osaka, Japan is designing a high resolution single photon emission computed tomography (SPECT) imager for obtaining high resolution brain scans for various imaging diagnostic applications. The camera consists of one large field of view detector imaging the whole brain and multiple smaller field of view high resolution detectors imaging small regions of the brain (see Fig. 1). The large field of view detector provides images without truncation that localize areas of particular diagnostic interest and provide support information for the reconstruction of high resolution regions of interest (ROIs) from high resolution truncated projections obtained with the small field of view detectors. The work presented in this paper develops an algorithm that accurately reconstructs uniformly attenuated truncated projections, which is an extension of the interior reconstruction problem for the reconstruction of non attenuated truncated projections.

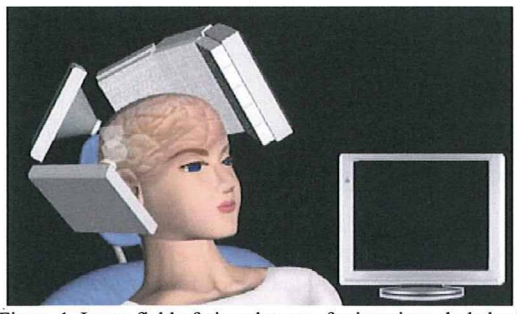

Figure 1. Large field of view detector for imaging whole brain and smaller field of view detectors for imaging ROIs.

The Department of Investigative Radiology has been involved in a large-scale multicenter clinical study aimed at evaluating validity and impact of a quantitative SPECT reconstruction package (QSPECT) [1] for multicenter clinical studies. The quantitative SPECT reconstruction package provides quantitative functional parametric images which are consistent among different setup of equipments and institutions. This allows the use of SPECT in a large scale clinical evaluation for diagnosing brain autoregulatory abnormalities. (A review of noninvasive diagnostic tests to assess cerebral autoregulation can be found in [2].) Dynamic SPECT scans are used to quantify cerebral blood flow (CBF) and cerebral vascular reactivity (CVR) in a single session using a split dose administration of ^{123}I iodo-amphetamine (IMP); one at rest and one during Diamox challenge [3]. Clinical data using QSPECT demonstrated that CBF at rest and during Diamox was reproducible among institutions.

This work was supported in part by the National Institutes of Health under Grant R01 EB00121, and in part by the Director, Office of Science, Office of Biological and Environmental Research, Medical Sciences Division of the U.S. Department of Energy under Contract DE-AC02-05CH11231.

Qiu Huang is with Lawrence Berkeley National Laboratory, One Cyclotron Road, MS 55R0121, Berkeley, CA 94720-8119. (phone: 510-495-2714; fax: 510-486-4768; e-mail: qhuang@lbl.gov).

Tsutomu Zeniya is with the National Cardiovascular Center Research Institute, Suita, Osaka, Japan (e-mail: zeniya @ri.ncvc.go.jp).

Hiroyuki Kudo is with University of Tsukuba, Tsukuba, Japan (e-mail: kudo@*is*.tsukuba.ac.jp).

Hidehiro Iida is with the National Cardiovascular Center Research Institute, Suita, Osaka, Japan (e-mail: iida@ri.ncvc.go.jp).

Grant T. Gullberg is with Lawrence Berkeley National Laboratory, One Cyclotron Road, MS 55R0121, Berkeley, CA 94720-8119. (e-mail: gtgullberg@lbl.gov).

Another important part of the multi-center trial is to evaluate neuronal damage due to ischemia and to provide prognostic value for surgical outcomes. Damage of benzodiazepine receptors has been found in cases of patients with severe brain ischemia [4]. Also, alterations of central benzodiazepine receptors have been described in several neuropsychiatric conditions, including epilepsy, Alzheimer's disease, Huntington's chorea and schizophrenia. Carbon-11-flumazenil, a benzodiazepine antagonist, has been used as a PET radiotracer for visualization and quantification of benzodiazepine receptors in humans. Recently, an iodinated analog of flumazenil, iomazenil has been introduced as a SPECT radiotracer. SPECT imaging of iodine-123-iomazenil (Iomazenil) binding to benzodiazepine receptors in the brain is being used to evaluate neuronal damage caused by ischemia [4] and the prognosis prior to carotid endoarterectomy [5]. Kinetic model-based methods have been developed for SPECT to quantitatively measure ^{123}I-iomazenil binding to benzodiazepine receptors in the human brain [6].

The Department of Investigative Radiology is developing a camera that will perform high resolution imaging of local ROIs in the brain to better address these imaging applications. Imaging with a high resolution small field of view camera provides truncated projections. The reconstruction of these projections involves determining the solution to the interior problem in local tomography. The interior problem in medical imaging refers to the situation where the region-of-interest (ROI) is totally contained within the object. For instance, in SPECT, the interior problem happens when the projections passing through the region outside the ROI are truncated due to a small field-of-view detector or a short detector-to-object distance in the case of converging collimation. The interior problem has been studied for some time [7]. Recently, Kudo *et al.* [8] proved that the solution is unique and stable in computed tomography (CT) if a small region in the ROI is known *a proiri*. In this paper this result is extended to the SPECT interior reconstruction problem.

Both in the work of Kudo *et al.* and in the work presented in this paper, the theory for the solution to the interior problem is based on the differentiation backprojection (DBP) method. The concept of DBP was first developed in parallel beam [9] and cone-beam [10] geometry in CT. The non interior truncation problem was solved for CT in [11], [12], [13], [14], [15]. Similar works in SPECT can be found in [16], [17], [18], [19], [20], where uniform attenuation was assumed. In SPECT the assumption of uniform attenuation is reasonable for some applications such as in brain imaging [21]. The result of the work in this paper shows that, with *a proiri* information of the ROI, the brain image can be reconstructed even when the imaging geometry forms an interior problem. It is expected that this result is useful in the reconstruction of pinhole data, where a pinhole collimator is attached to the small field-of-view cameras for imaging the brain. The pinhole collimator provides a small field-of-view (FOV) with high sensitivity and high resolution when located close to the object.

The paper is organized as follows: Section II shows that the differentiated backprojection (DBP) of fan-beam data is related to the distribution of the radioactive tracer in SPECT through a truncated weighted Hilbert transform. Then a unique inversion is shown to exist for the truncated weighted Hilbert transform given a small region of ROI is known *a proiri*. The results of numerical simulations are presented in Section III where the theory is shown to give a measure of confidence for the quantitative accuracy of the fan-beam reconstruction problem and the conclusion is given in Section IV.

II. Method

The method in this work is illustrated by showing that the differentiated backprojection (DBP) of fan-beam data is related to the distribution of the radioactive tracer in SPECT through a truncated weighted Hilbert transform and the truncated weighted Hilbert transform can be inverted given some prior information.

A. DBP operation for fan-beam data

For a transaxial slice, let $f(x,y)$ represent the distribution of the radiopharmaceutical in body tissues, which is assumed to be a smooth and compactly supported function of R^2. The SPECT image reconstruction estimates $f(x,y)$ from the detected photon counts. We denote $\vec{r}=(x,y)$ and $D=\{(x,y)\in R^2:\ x^2+y^2\le 1\}$. We assume $f(x,y)\equiv 0$ outside of D and the attenuation μ of the body tissues is uniform inside D. A typical fan-beam data acquisition geometry with a circular focal-point trajectory is shown in Fig. 2, where each projection ray is represented by (β,σ). One particular projection ray is shown emanating from the focal point S for the angle β with the ray angle σ.

In this paper, the fan-beam uniformly attenuated projection of the function $f(x,y)$ is defined as

$$[D_\mu f](\beta,\sigma)=\int_0^\infty f(S+\tau\vec{\alpha}(\beta,\sigma))e^{\mu\tau}d\tau\,, \qquad (1)$$

where $D_\mu f$ is the projection operator for the uniformly attenuated fan-beam projection data, $\sigma\in[-\sigma_m,\sigma_m]$, and $\vec{\alpha}(\beta,\sigma)$ is a unit vector in R^2 representing the direction from the focal point to the collimation hole, as shown in Fig. 2. Here, $\sigma_m\in(0,\pi/2)$ denotes the maximum angle subtended by the fan-beam. Let R be the radius of the circular focal point trajectory. We can modify the fan-beam data to obtain:

$$g(\beta,\sigma)=e^{-\mu R\cos\sigma}[D_\mu f](\beta,\sigma)\,. \qquad (2)$$

Define

$$s=R\sin\sigma,\quad \theta=\sigma+\beta$$

$$\hat{\sigma}(r,\varphi,\theta)=\arcsin\frac{\vec{r}\cdot\vec{\theta}}{R}=\arcsin\frac{r\cos(\theta-\varphi)}{R}\,.$$

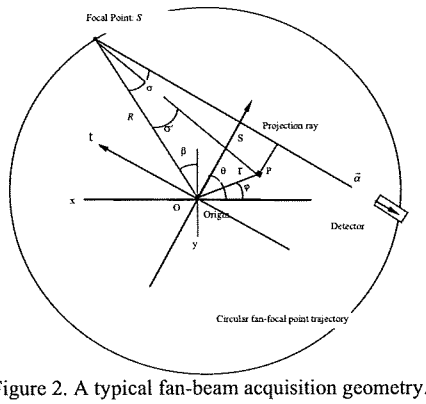

Figure 2. A typical fan-beam acquisition geometry.

We denote $\vec{\theta} = (\cos\theta, \sin\theta)$ and $\vec{\theta}^{\perp} = (-\sin\theta, \cos\theta)$ and construct an image:

$$\hat{f}(x,y) = -\frac{1}{2}\int_{-\pi/2}^{\pi/2} \frac{e^{t\vec{\omega}\cdot\vec{\theta}^{\perp}}[(\frac{\partial}{\partial\sigma}-\frac{\partial}{\partial\beta})g](\theta-\hat{\sigma}(r,\varphi,\theta),\hat{\sigma}(r,\varphi,\theta))}{R\cos\hat{\sigma}(r,\varphi,\theta)}d\theta. \quad (3)$$

This image was proved to be related to the original distribution of radiopharmaceutical as [17]:

$$\hat{f}(x,y) = \int_{-\infty}^{\infty} \frac{\cosh(\mu\tau)f(x-\tau,y)}{\pi\tau}d\tau. \quad (4)$$

Equation (3) involves the operations of derivative and backprojection for the modified attenuated projection in fan-beam geometry and can be readily obtained from fan-beam measurements. Equation (4) shows that the image $\hat{f}(x,y)$ is an image obtained by convolving the true image with a one-dimensional (1D) kernel $\cosh(\mu t)/(\pi t)$ multiplied by some factor, thus the image reconstruction is accomplished by inverting the convolution corresponding to a truncated weighted Hilbert transform.

B. *Inversion of Truncated Hilbert Transform*

Denote the left hand side of (4) by $g(t)$ and the distribution of activity by $f(t)$. The reconstruction is to solve the following integral equation:

$$g(t) = \int_{-1}^{1} \frac{\cosh(\mu\tau)f(t-\tau)}{\pi\tau}d\tau.$$

As shown in Fig. 3, the function $f(t)$ has a support in $-1<t<1$. There is no loss of generality since shifting and scaling can always transform any support interval to $(-1,1)$.

If $g(t)$ is known for $-1<t<1$, the equation can be solved as in [19] and [17]. Unfortunately, for some geometries the function $g(t)$ is only available on a small interval $-1<a<t<d<1$. Then the algorithms in [19] and [17] do not guarantee a stable inversion. However, based on the work by Kudo et al [8], we

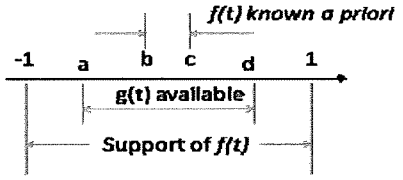

Figure 3. Illustration of intervals.

found if the value of $f(t)$ in the interval $a<b<t<c<d$ is assumed to be known, then the inversion is available in (a,d).

The reconstruction problem becomes:

$$g(t) = \int_{-1}^{1} \frac{\cosh(\mu\tau)f(t-\tau)}{\pi\tau}d\tau \quad . \quad (-1<a<t<d<1), \quad (5)$$

subject to $f(t) = f^{(p)}(t)$ for $(a<b<t<c<d)$.

According to [17], we know the inversion can be obtained by constructing a new function from $g(t)$:

$$\int_{-1}^{1} \frac{g(s)}{\pi(s-t)}\frac{\sqrt{1-t^2}}{\sqrt{1-s^2}}ds.$$

In this case, this function can be broken into two terms: $h_1(t)+h_2(t)$, where

$$h_1(t) = \int_{a}^{d} \frac{g(s)}{\pi(s-t)}\frac{\sqrt{1-t^2}}{\sqrt{1-s^2}}ds,$$

$$h_2(t) = \left(\int_{-1}^{a} . + \int_{d}^{1} .\right)\frac{g(s)}{\pi(s-t)}\frac{\sqrt{1-t^2}}{\sqrt{1-s^2}}ds.$$

The first term $h_1(t)$ is available from the truncated weighted Hilbert transform $g(t)$ for $a<t<d$, while the second term $h_2(t)$ remains unknown.

Since the function $f(t)$ is known for $b<t<c$, the second term in this interval can be represented as

$$h_2(t) = \left[\left((I+\Phi)f^{(p)}\right)\right](t) - h_1(t) \qquad \text{for} \qquad t\in(b,c).$$

Here, the operator Φ is the same as in [17] and I indicates the unity operator.

According to the continuity property of analytical functions, the function $h_2(t)$ can be analytically continued from the known interval (b, c) on the real axis to the larger interval (a, d) on the real axis. Since both $h_1(t)$ and $h_2(t)$ are uniquely determined for $t\in(a,d)$, function $f(t)$ is uniquely determined for $t\in(a,d)$. Then the projection onto convex sets (PCOS) method [22] was used to solve the integral equation in (5). Numerical results will be shown in the next section.

III. Numerical Results

In the fan-beam SPECT simulation study, the object image is chosen to be the modified Shepp-Logan phantom shown in Fig. 4. Uniform attenuation coefficient $\mu=0.15cm^{-1}$ was chosen to generate the truncated attenuated fan-beam data.

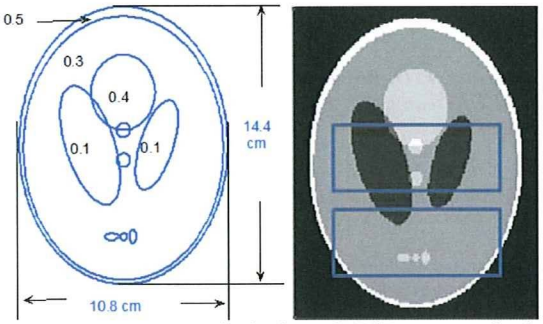

Figure 4 Digital phantom for fan-beam SPECT computer simulation. The square boxes in the right image indicate two regions-of-interest (ROIs).

In the reconstruction, first, differentiation followed by backprojection of truncated SPECT data was obtained. Then assuming the activity within a small part of the region-of-interest is known, the other part of the ROI was estimated using the PCOS method. The reconstructed image is shown in Fig. 5.

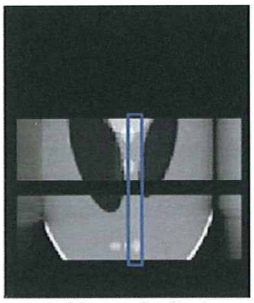

Figure 5: The reconstructed image for fan-beam geometry. The box indicates the region where the distribution is known *a priori*.

IV. Conclusion

This paper extended the work in [8] to SPECT imaging where uniform attenuation map is assumed. The interior problem was shown to be solvable given tiny *a priori* information. Reconstructions from simulated fan-beam data verify the theory.

The investigation of a pinhole system is presently undergoing. In the pinhole simulation, regularized maximum *a posteriori* (MAP) algorithm is used to reconstruct the simulated pinhole data. A low resolution reconstruction of the parallel beam collimated data is used as prior information.

References

[1] Iida H, Hayashida K, Nakazawa M and Katabuchi T, "Multicenter evaluation of quantitative SPECT reconstruction package – QSPECT & DTARG," *J. Nucl. Med.* 47 (Supplement 1), pp. 121, 2006.

[2] Rudzinski W, Swiat M, Tomaszewski M and Krejza J, "Cerebral hemodynamics and investigations of cerebral blood flow regulation," *Nucl Med Rev*, vol. 10, pp. 29-42, 2007.

[3] Imaizumi M, Kitagawa K, Hashikawa K, Oku N, Teratani T, Takasawa M, Yoshikawa T, Rishu P, Ohtsuki T, Hori M, Matsumoto M and Nishimura T, "Misery perfusion with split-dose ^{123}I-iodoamphetamine single-photon emission computed tomography in patients with carotid occlusive diseases," *Stroke*, vol. 33, pp. 2217-2223, 2002.

[4] Moriwaki H, Matsumoto M, Hashikawa K, Oku N, Ishida M, Seike Y, Fukuchi K, Hori M and Nishimura T, "Iodine-123-iomazenil and iodine-123-Iodoamphetamine SPECT in major cerebral artery occlusive disease," *J Nucl Med*, vol. 39, pp. 1348-1353, 1998.

[5] Tsuchida T, Yonekura Y, Sadato N, Takahashi N, Yamamoto K and Ishii Y, "Prediction of improvement of cerebral perfusion with I-123 iomazenil SPECT," *Annals of Nucl. Med.*, vol. 13, pp. 265-268, 1999.

[6] Dargham A, Larulle M, Seibyl J, Rattner Z, Baldwin R M, Zoghbi S S, Zea-Ponce Y, Bremner J D, Hyde T M, Charney D S, Hoffer P B and Innis R B, "SPECT measurement of benzodiazepine receptors in human brain with iodine-123-iomazenil: kinetic and equilibrium paradigms," *J. Nucl. Med.*, vol. 35, pp. 228-238, 1994.

[7] Natterer F, *The Mathematics of Computerized Tomography* (SIAM), 1986.

[8] Kudo H, Courdurier M, Noo F and Defrise M, "Tiny *a proiri* knowledge solves the interior problem in computed tomography," *Phys. Med. Bio.*, vol. 53, pp. 2207-2231, 2008.

[9] Noo F, Clackdoyle R and Pack J D, "A two-step Hilbert transform method for 2D image reconstruction," *Phys. Med. Biol.*, vol. 49, pp. 3903-3923, 2004.

[10] Zou Y and Pan X, "Exact image reconstruction on PI-lines from minimum data in helical cone-beam CT," *Phys. Med. Biol.*, vol. 49, pp. 941-959, 2004.

[11] Pack J D, Noo F and Clackdoyle R, "Cone-beam reconstruction using the backprojection of locally-filtered projections," *IEEE Trans. Med. Imag.*, vol. 24, pp. 70-85, 2005.

[12] Pack J D and Noo F, "Cone-beam reconstruction using 1D filtering along the projection of M-lines," *Phys. Med. Biol.*, vol. 49, pp. 2317-2336, 2004.

[13] Ye Y and Wang G, "Filtered backprojection formula for exact image reconstruction from cone-beam data along a general scanning curve," *Med. Phys.*, vol. 32, pp. 42-48, 2005.

[14] Zou Y and Pan X, "Image reconstruction on PI-lines by use of filtered backprojection in helical cone-beam CT," *Phys. Med. Biol.*, vol. 49, pp. 2717-2731, 2004.

[15] Zou Y and Pan X, "An extended data function and its generalized backprojection for image reconstruction in helical cone-beam CT," *Phys. Med. Biol.*, vol. 49, pp. N3837, 2004.

[16] Huang Q, You J, Zeng G L and Gullberg G T, "Exact Reconstruction From Uniformly Attenuated Helical Cone-Beam projections in SPECT," LBNL Technical Report, LBNL-1359E, Lawrence Berkeley National Lab, Berkeley, USA., 2008.

[17] Huang Q, You J, Zeng G L, and Gullberg G T, "Reconstruction from uniformly attenuated SPECT partial-scan projection data using DBH method," IEEE Trans. Med. Imag., vol. 28, pp. 17-29, 2009.

[18] Noo F and Pack J D, "Theory for image reconstruction from divergent beam projections in SPECT," *IEEE Nuclear Science Symposium Conference Record*, vol. 6, pp. 3449-3452, 2006.

[19] Noo F, Defrise F, Pack J and Clackdoyle R, "Image reconstruction from truncated data in SPECT with uniform attenuation," *Inverse Problems*, vol. 23, pp. 645-667, 2007.

[20] Rullgard H, "An explicit inversion formula for the exponential Radon transform using data from 180 degrees," (Preprint in 2002 Sep) *Ark. Math.*, vol. 42, pp. 353-362, 2004.

[21] Liang Z, Ye J and Harrington D P, "Quantitative brain SPECT in three dimensions: an analytical approach without transmission scans," *Three-Dimensional Image Reconstruction in Radiology and Nuclear Medicine*, Kluwer Academic Publishers, pp. 117-132, 1996.

[22] Youla D C and Webb H, "Image restoration by the method of convex projections: Part I. Theory," *IEEE Trans Med. Imag.*, vol. 1, pp. 81–94, 1982.

A method to measure PET scatter fractions for daily quality control

H. W. de Jong[a)]
Department of Radiology and Nuclear Medicine, University Medical Centre, P. O. Box 85500, 3508 GA, Utrecht, The Netherlands and Department of Nuclear Medicine and PET Research, VU University Medical Centre, P. O. Box 7057, 1007 MB, Amsterdam, The Netherlands

M. Lubberink
Department of Nuclear Medicine and PET Research, VU University Medical Centre, P. O. Box 7057, 1007 MB, Amsterdam, The Netherlands

H. Watabe and H. Iida
Department of Investigative Radiology, National Cardiovascular Center Research Institute, 5-7-1 Fujishirodai, Suita, Osaka 565-8565, Japan

A. A. Lammertsma
Department of Nuclear Medicine and PET Research, VU University Medical Centre, P. O. Box 7057, 1007 MB, Amsterdam, The Netherlands

(Received 25 March 2009; revised 27 July 2009; accepted for publication 29 July 2009; published 14 September 2009)

Purpose: Regular monitoring of PET scanner performance is mandatory to assure quality of acquired data. While extensive performance measurements include many scanner characteristics such as resolution, count rate, uniformity, sensitivity, and scatter fraction (SF), most daily QC protocols are limited to uniformity and sensitivity measurements. These measurements may be too insensitive to detect more subtle drifts in detector gains that could lead to reduced detection of primary and increased detection of scattered events. Current methods to measure SF, such as those prescribed by the NEMA protocols (SF-NEMA), however, require specially designed phantoms and are too cumbersome to be performed on a daily basis.
Methods: In this study, a simple and versatile method to determine SF is described. This method (SF-DAILY) does not require additional measurements, making it suitable for daily QC. The method was validated for four different scanners by comparing results with those obtained with the NEMA 1994 protocol.
Results: For all scanner types and acquisition modes, excellent agreement was found between SF-NEMA and SF-DAILY.
Conclusions: The proposed method is a very practical and valuable addition to current daily QC protocols. In addition, the method can be used to accurately measure SF in phantoms with other dimensions than the NEMA phantom. © *2009 American Association of Physicists in Medicine.* [DOI: 10.1118/1.3213096]

Key words: PET, scatter fraction, quality control, NEMA

I. INTRODUCTION

Assessment of PET scanner performance is mandatory to prevent image artifacts and to assure quantitative integrity of acquired data. In general, extensive performance measurements are performed only occasionally, e.g., after scanner installation, an upgrade, or major maintenance, with more concise quality control (QC) measurements being performed on a daily basis (daily QC). The purpose of this daily QC is to detect scanner malfunctioning and to monitor scanner stability. Ideally, this daily QC should be sensitive enough to detect changes in scanner performance that require (immediate) attention. As scanner maintenance may have substantial impact on patient throughput and planning, however, a decision to perform maintenance should be well founded, preferably based on a more extensive set of measured parameters. Therefore, it is important that daily QC tests provide as much relevant information as possible. Apart from offering a solid basis for decision making in clinical practice, daily QC data can also give insight in scanner behavior as a function of temperature, power loss, or time after maintenance.

While the above mentioned extensive (acceptance) performance measurements (using a range of different phantoms) include many scanner characteristics such as uniformity, sensitivity, and scatter fraction (SF), for practical reasons, the daily QC often is restricted to detector uniformity and sensitivity. These parameters are typically derived from a scan of a uniform cylindrical phantom filled with the long-lived isotope ^{68}Ge. These limited measurements may, however, obscure scanner drift or inaccuracies caused by changing detector gains, possibly leading to reduced detection of primary and increased detection of scattered events. In addition, drifts in electronics settings can lead to loss of sensitivity. For example, a shift in photomultiplier tube (PMT) gains can cause the 511 keV photopeak to drift, eventually (partly) falling outside the energy window.[1] This, in turn, may lead to a direct change in the detected SF, and hence image quality

and quantitative accuracy. Especially in state-of-the-art PET scanners that can only operate in 3D mode, SF is high (typically 50% of all detected events) and alterations in measured SF can have a major impact. In order to quantify 3D PET data, sophisticated scatter correction algorithms have been developed. If adjustments are not made while needed, however, changes in SF can cause the algorithm to over- or underestimate the scatter contribution, leading to bias, i.e., incorrect regional activity concentrations.

The SF is defined as the fraction of all events that have been scattered prior to detection. There are many ways to determine this SF, but the most widely accepted method is according to the NEMA standards. NEMA protocols have been established in a collaboration between scanner manufacturers and users. The advantage of NEMA protocols is that results can be interpreted by all parties, without uncertainties about the exact conditions under which measurements were performed. This is especially useful when communicating results between users, manufacturers, or other parties. Disadvantages of NEMA protocols are that they usually require specially designed setups and phantoms and that they are too cumbersome for use on a daily basis. Consequently, NEMA protocols often are used only for acceptance testing and in other situations where extensive measurements are required (e.g., following a major upgrade).

The purpose of the present study was to develop and validate a simple method to accurately estimate scatter fractions using a uniform cylindrical phantom. In general, a uniform cylindrical phantom is used to monitor sensitivity and uniformity on a daily basis and, therefore, this SF method could easily be added to the daily or weekly QC without the need for additional measurements. Validation was performed by comparing measured SF values with those derived according to the NEMA NU-1994 protocol using four different scanners.

II. MATERIALS AND METHODS

II.A. NEMA scatter fraction

NEMA standards for PET instrumentation describe a series of phantom measurements to determine scanner characteristics, including spatial resolution, scatter fraction, count rates, sensitivity, accuracy of correction methods, and general image quality. While the older NEMA-1994 protocol[1,2] was defined in a time when PET was primarily used as a brain imaging modality, the 2001 and 2007 protocols reflect the shift toward whole-body oncological applications.[3–6] For the SF measurement this is illustrated by the short 20 cm cylinder in the NEMA 1994 protocol (SF-NEMA1994) and the longer 70 cm cylinder in the NEMA 2001 protocol (SF-NEMA2001). The latter phantom was introduced to include scatter that originates from outside the axial field of view (FOV) of the scanner, and therefore SF-NEMA2001 is higher than SF-NEMA1994, especially when scanning in 3D mode (i.e., without septa in the FOV). In a comparative study, however, it was shown that a change in SF-NEMA1994 strongly correlated with a change in SF-NEMA2001.[3]

As the cylindrical daily QC phantom often has the same dimensions as the NEMA1994 scatter fraction phantom, SF-NEMA1994 was used as the gold standard for validating the proposed method. The NEMA1994 protocol describes a 20 cm diameter, 20 cm length, water filled cylinder in which a 20 cm line source can be inserted at three different positions (0, 45, and 90 mm from the center) (Fig. 1). After filling the line source with a low level of activity (~5 kBq/cc of ^{18}F), it was inserted at each of the three positions and, at each position, data were acquired for 15 min to ensure at least 200 kcounts per slice within the central 17 cm of the phantom.

SF-NEMA1994 was then obtained by (1) correcting the three measurements for ^{18}F decay, detector nonuniformities (normalization), and, where relevant, detector gaps (Fig. 1), (2) straightening the sinograms to eliminate curves due to off-center line source positions (Fig. 1), (3) setting all sinogram pixels corresponding to positions >12 cm from the center of the phantom to zero, (4) adding projection angles to create one profile per line source position, and (5) adding the three scatter profiles, thereby weighting for the annular region in which the line source is positioned, where (6) scattered events under the primary peaks were estimated using linear interpolation between count levels within 2 cm from the peak[2] (Fig. 1).

II.B. Simplified procedure

When acquiring PET data using a uniform cylindrical phantom of diameter D, filled with an arbitrary activity and placed centrally in the FOV, the resulting total count (T) projections are the sum of primary (or unscattered) events (P), scattered events (S), and random events. In general, randoms are corrected for by subtracting an independently measured estimate, usually obtained with the delayed window technique and therefore not addressed specifically in this study.[7] If r is the position on the projection (bin position) relative to the center of the FOV, then $S(r)$ is an arbitrary function describing the scatter background. The point spread function PSF(r) is a 1D function describing the resolution of the projection data centered around $r=0$ (Fig. 2). It is now postulated that, for a nonoblique projection plane, the spatial distribution of the total counts T of primary and scattered events within the FOV of a single ring of detectors (or nonoblique, direct plane) originating from a cylindrical phantom with diameter D is given by

$$T(r) = \mathrm{PSF}(r) \otimes (P(r,D,p) + S(r)),$$

$$P(r,D,p) = 2\sqrt{\frac{1}{4}D^2 - r^2} \cdot p \cdot \exp\left(-\mu\sqrt{\frac{1}{4}D^2 - r^2}\right), \quad r \le D,$$

$$P(r,D,p) = 0, \quad r > D, \tag{1}$$

where μ is the linear attenuation coefficient at 511 keV (cm^{-1}), $P(r,D,p)$ describes the distribution of the detected primary photons, and p is a scaling factor for the total number of detected primary photons that depends on both activity

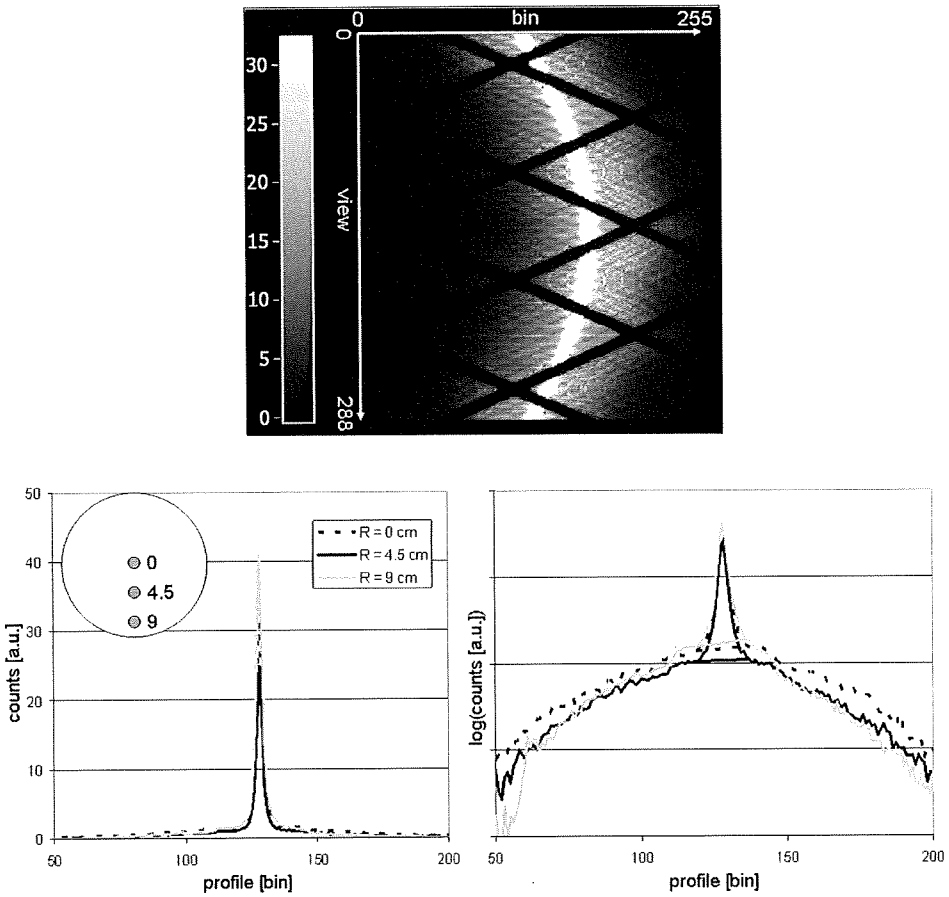

FIG. 1. Illustration of SF-NEMA procedure. The top image shows a sinogram from a line measurement for one of the three positions. Line profiles (bottom) are generated by straightening the profiles and averaging all views of the sinogram. Profiles are also shown using a logarithmic scale including the interpolated curves between ±2 cm (this case ±16 bins) from the center for scatter estimation. Using these curves primary and scatter fractions are extracted by integrating the profiles as described by the NEMA protocol.

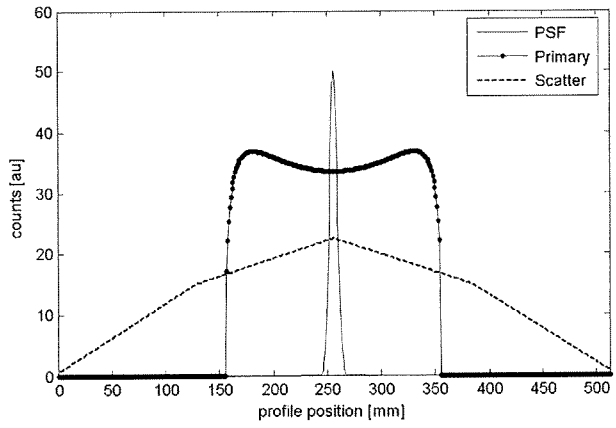

FIG. 2. Example of the three parts of the model used for estimating the SF-Daily: A PSF with a FWHM of 7 mm (scaled for illustration purposes), a primary response from a cylinder with a diameter of 20 cm, and an arbitrary scatter response.

in the phantom and sensitivity of the scanner. In short, the total response is a sum of primary and scatter events, where the shape of the primary contribution is known. In this case the activity of the nonoblique cross section through the cylindrical phantom was approximated by a circle [first term of $P(r,D,p)$], and multiplication with the attenuation factor (last exponential term) estimates the shape of the response in the absence of scattered photons.

In this study $S(r)$ was modeled as a first order cubic spline[8] based on a set of control points $(r_1,y_1;\ldots;r_n,y_n)$, i.e., $S(r)$ was simply modeled as a piecewise linear function between the coordinates (r_1,y_1) and (r_2,y_2), (r_2,y_2) and (r_3,y_3), and so on. Although a piecewise linear shape might not be natural, the convolution with PSF(r) removes discontinuities at the control points. Figure 2 gives an example of the components $P(r)$, $S(r)$, and PSF(r).

The new simplified method to derive SF (SF-Daily) makes direct use of Eq. (1). First, the PSF is modeled using a Gaussian function with a fixed width based on scanner specific resolution data. For the sake of simplicity, in all cases a spatially invariant resolution was assumed. Next, for the scatter function $S(r)$, the control points are chosen

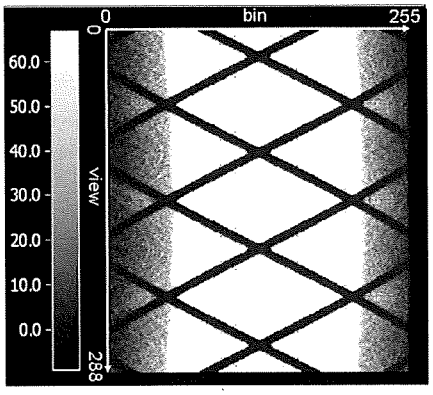

FIG. 3. Sinogram of uniform cylinder used for daily QC measurements. Scatter in the background of the sinogram is clearly visible. Black diagonal lines are due to gaps between detectors heads

equally divided over the data space (r direction) with r_1 located at the beginning and r_n at the end of the transversal field of view. For this study five control points were used. Since D, μ, and PSF(r) are known and $r_1,\ldots,r_5$ are fixed, $T(r)$ has p and the five base points $y_1,\ldots,y_5$ as free parameters. These parameters were estimated by fitting $T(r)$ to a measured response projection profile using a nonlinear curve fitting method (Levenberg-Marquardt[9]). It should be emphasized here that Eq. (1) is fitted to all projection data and not just to the tails of the sinogram, making the method very robust. For calculating SF only counts in the region $r \pm 3/5D$ are taken into account as this is prescribed by the NEMA protocol:

$$\mathrm{SF} = \frac{\int_{-3/5D}^{3/5D} S(r)dr}{\int_{-3/5D}^{3/5D} T(r)dr}. \tag{2}$$

To acquire data, a uniformly filled cylindrical phantom with known diameter (in the present case 20 cm for the whole-body scanners and 4.5 cm for the animal scanner) has to be placed in the center of the FOV, with its long axis in line with the scanner axis. In case the scanner has scintillation crystals containing intrinsic radioactivity such as L(Y)SO, background radiation has to be taken into account, as it produces randoms and a small fraction of true coincidences due to cascading gamma rays.[10] This background activity, however, usually is very low (typically less than 1×10^{-5} counts per second per line of response). On the other hand care should be taken not to induce pileup effects that can alter SF due to high count rates. Although this differs from scanner to scanner, as an example, SF for the high resolution research tomography (HRRT) is stable when total activity in the FOV is between approximately 1 and 100 MBq.[11] Although the count rate has negligible effect on SF as long as it is kept within the clinical range, ideally, total activity in the cylinder should be comparable to that used for the NEMA protocol (2.5 kBq cc^{-1}, or 15 MBq). Figure 3 shows an example of an acquired sinogram.

II.C. Scanners

To test and validate the new SF-Daily method under various circumstances, data from four different PET scanners were used. The scanners varied in crystal material, crystal size, ring diameter, and axial field of view, characteristics that all affect the scatter fraction. Table I gives an overview of relevant scanner data.

The Siemens HR (also known as ECAT Exact 47)[12] is a whole-body BGO scanner that can be operated in both 2D and 3D modes by means of retractable septa. Although 3D acquisitions yield higher sensitivity, the 2D mode is characterized by smaller randoms and scatter fractions, which can be advantageous for high count rate studies. The Philips Allegro[13] is a 3D only whole-body scanner based on curved GSO crystals, which have the advantage of a relatively high energy resolution compared with other PET crystals, resulting in a lower SF. The 3D only Siemens HRRT was one of the first scanners to apply LSO crystals. Its high spatial resolution enables detailed brain studies and small animal applications that can be covered in one bed position, thanks to the large axial FOV.[11] The Siemens microPET Focus 120 (Ref. 14) is a dedicated small animal LSO scanner with a gantry opening of approximately 20 cm. Although a new NEMA protocol specifically for small animal PET scanners was introduced only recently[15] microPET experiments using NEMA-like phantoms have already been reported previously.[16] Table I also lists resolution data (mm FWHM) as used for modeling PSF in Eq. (1).

II.D. Scatter fraction measurements

SF-NEMA and SF-Daily were measured and compared for all four scanners. For the HR, SF was measured using a cylinder, filled with ^{18}F, in both 2D and 3D acquisition modes. This provided a means to evaluate the effects of septa on measured SF for both methods. Although in most cases 3D sinograms were acquired, analysis was performed only on nonoblique (direct) planes in the sinogram. Hence, all

TABLE I. Relevant data of the various scanners.

Scanner	Crystal material	Crystal thickness (mm)	Axial FOV (cm)	Diameter gantry (cm)	Resolution used (mm FWHM)	Ring diameter (cm)
Siemens HR	BGO	30	15	51	5	82.7
Philips Allegro	GSO	20	18	56	5	86.4
Siemens HRRT	LSO	20	25	31	3	46.9
Siemens microPET Focus 120	LSO	10	7.6	20	2	25.8

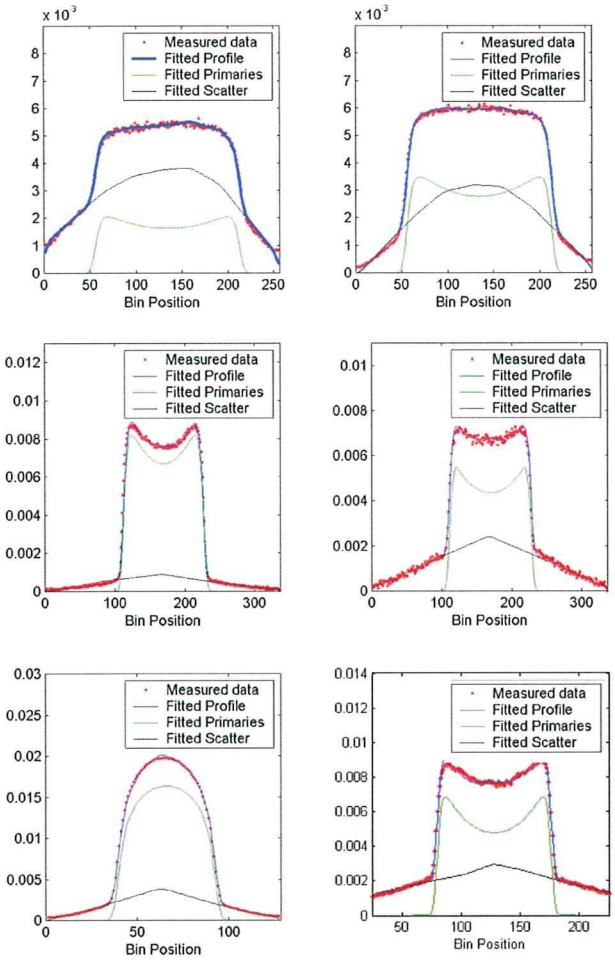

FIG. 4. Profiles of measured and fitted data. Top: HRRT before (left) and after (right) scanner setup. Mid: HR in 2D (left) and 3D (right) acquisition mode. Bottom: MicroPET (left) and Allegro (right). Due to the normalization process vertical units are arbitrary.

oblique planes (also called segment 1 and higher) were disregarded, effectively resulting in a 2D sinogram.

For the HRRT, SF-Daily was measured using a ^{68}Ge phantom (diameter of 20 cm, length of 27 cm, 20 MBq), routinely used for daily QC purposes. Sensitivity of SF-NEMA to small changes in SF was investigated by measuring SF of the HRRT just before and after performing a setup process (i.e., tuning of gain and other settings in order to maximize performance), as this setup process will decrease SF due to optimized energy calibration. SF was measured for the whole gantry and plane by plane. To assess effects of noise, SF-Daily for the whole gantry was measured using acquisition times of 15, 2, and 1 min.

For the Allegro, SF was determined for different lower energy threshold settings (260, 310, 360, and 410 keV) and an upper level discriminator set to 665 keV in order to investigate the correlation between both SF methods. For this a 20 cm diameter, 20 cm length cylinder filled with 20 MBq ^{18}F was used. As no mini-scatter-phantom was available for the microPET Focus 120, only SF-Daily was measured using a cylinder with an inner radius of 4.5 cm and a length of 10 cm, filled with 10 MBq, and this measurement was compared with published SF-NEMA values.[4]

TABLE II. Comparison of SF-NEMA and SF-Daily.

Scanner	SF-NEMA (%)	SF-Daily (%)
HRRT before setup	63	63
HRRT after setup	50	51
HRRT 15 min	50	51
HRRT 2 min	50	50
HRRT 1 min	50	50
HR 2D	14	13
HR 3D	38	33
MicroPET 45mm diameter cylinder	27[a]	23
Allegro	36	34

[a]The SF-NEMA was determined for a 60 mm phantom (8).

III. RESULTS

Sinogram profiles of the central axial plane and SF-Daily curve fits of total response $T(r)$ according to Eq. (1) are shown in Fig. 4 for all scanners. In addition, resulting primary $P(r)$ and scattered events $S(r)$ are shown. In all cases, the analytical response function equation (1) could be fitted to the data with high accuracy. Clearly, both shape and amplitude of the scatter distribution differ among scanners and acquisition modes. The HRRT setup process resulted in a lower SF and a more symmetric scatter distribution. Differences in scatter contribution between 2D and 3D modes are clearly illustrated by the HR profiles. The HR in 3D mode and the Allegro (measured using the lower level discriminator set at 410 keV) have similar profiles, indicating the impact of scanner geometry. The shape of the fitted primaries of the microPET deviates substantially from that of the other scanners due to the much smaller size of the phantom used. In general, SF measurement using SF-Daily were relatively insensitive to changes in PSF. Typically, doubling PSF (e.g., from 5 to 10 mm) resulted in only a 10% change in SF-Daily.

Table II summarizes SF values as obtained with SF-Daily and SF-NEMA. In addition, in case of the HRRT, SF values for different noise levels are included. Plane-by-plane SF values for the HRRT are shown in Fig. 5.

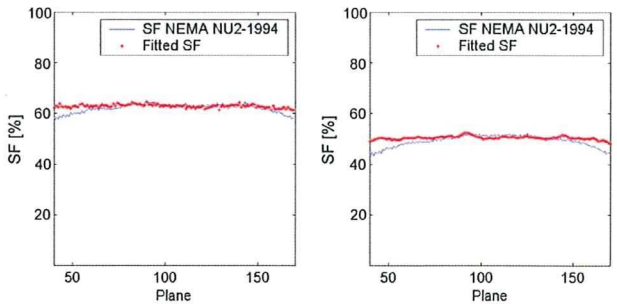

FIG. 5. Plane-by-plane values of SF-NEMA and SF-Daily (fitted SF) for the HRRT before (left) and after (right) setup.

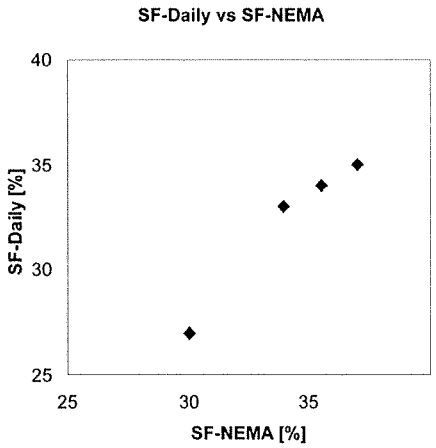

FIG. 6. SF-Daily and SF-NEMA values measured on the Allegro. Data points with higher SF refer to measurements with lower threshold values (260, 310, 360, and 410 keV).

Figure 6 shows SF values of the Philips Allegro for varying lower energy threshold settings. Both SF-NEMA and SF-Daily increased slightly with decreasing threshold channel, and a good correlation between both methods was found (R^2=0.96). Finally, Fig. 7 shows a Bland-Altman plot of the combined results presented in Table II and Fig. 6.

IV. DISCUSSION AND CONCLUSION

Using a simple curve fitting method, SF-Daily values were determined for different scanners and acquisition modes and compared to SF-NEMA values. A difference between SF-Daily and SF-NEMA only existed for the HR in 3D mode and for the microPET. For the latter, however, SF-Daily was measured using a cylinder with an inner diameter of 4.5 cm, while published SF-NEMA data were obtained with a cylinder of 6 cm diameter. The impact of noise was negligible for the three acquisition times investigated. The count rate in the HRRT scans was approximately 50 kcounts per slice, resulting in more than 100 counts per bin in the 1 min profiles, apparently sufficient for an accurate fit. The

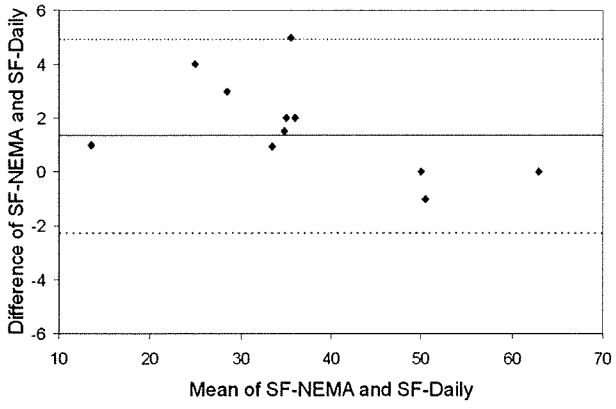

FIG. 7. Blant-Altman plot of all SF data from all four scanners and scan modes (data from Table II).

plane-by-plane comparison of SF-Daily and SF-NEMA showed good agreement especially in the center of the FOV. The slight deviation for the outer planes is probably due to the slightly longer phantom used for SF-NEMA than for SF-Daily.

In general, slight deviations in fitted and acquired profiles could be seen, especially at the maxima of the response (Fig. 4). Most likely these deviations are due to the fact that the thickness of the wall of the cylinder was not taken into account. Nevertheless, they have negligible effect on the resulting SF.

Similar to SF-NEMA, SF-Daily can be performed on either only a subset of the total sinogram, e.g., only on nonoblique (direct) planes, or on all sinogram planes/segments via a rebinning step.[5] The latter requires slight adaption of Eq. (1), as the primary response in oblique planes will be based on an oblique cross section of the phantom (in case of a cylinder this will become an ellipse) rather than a circle. In this study SF values were only determined using direct (2D) sinograms for both the SF-NEMA and SF-Daily methods. For one scanner these sinograms were derived from data acquired in both 2D mode (with septa) and 3D mode (without septa) in order to test different levels of scatter and randoms.

Although the SF-Daily method does require that the phantom is positioned in the center of the FOV, in practice it proved to be insensitive to slight misplacements. The method could, however, easily be extended with an algorithm to align the sinogram, similar to the SF-NEMA requirement.

One limitation is that not all scanners use cylindrical phantoms for daily QC purposes but rely on measurements of small sources in air. Although this has the benefit of requiring less activity, it gives the energy resolution at 511 keV rather than the scatter fraction. Furthermore, use of a point source in air also prohibits measurement of uniformity of coincidence timing over a large area of the FOV.

It should be emphasized that SF-Daily fits a profile to all projection data. This is in contrast to some scatter correction methods[17] that rely on fitting the tails of the scatter profile. In the presented approach all data are used and that knowledge about the primary response is included, making the method robust and insensitive to noise.

In general, SF-Daily values obtained were in close agreement with those derived using the NEMA protocol, making the method sufficiently sensitive to detect small changes in SF. Because the shape of the primary distribution is well known, accurate fits of the sum of scatter and primary events to the total profile can be achieved, without making prior assumptions about the shape of the scatter distribution. Furthermore no discontinuities in the estimated responses $S(r)$ were found. The method is also suitable for determining SF values in case of "dirty" radionuclides (i.e., radionuclides that emit gamma rays in addition to positrons),[18] activity outside the FOV, and phantoms with deviating dimensions, as long as the exact dimensions are known.

In conclusion, as this method does not require measurements with special phantoms, it can be used to accurately

monitor SF using both arbitrarily sized cylindrical phantoms and short acquisition times, making the method particularly useful for daily QC purposes.

[a]Author to whom correspondence should be addressed. Electronic mail: h.w.a.m.dejong@umcutrecht.nl; Telephone: +31-(0)88-7553327.

[1]G. Brix *et al.*, "Performance evaluation of a whole-body PET scanner using the NEMA protocol," J. Nucl. Med. **38**, 1614–1623 (1997).
[2]National Manufacturers Association, NEMA Standards Publication No. NU 2-1994 (National Manufacturers, Washington, DC, 1994).
[3]M. E. Daube-Witherspoon *et al.*, "PET performance measurements using the NEMA NU 2-2001 standard," J. Nucl. Med. **43**, 1398–1409 (2002).
[4]H. Herzog, L. Tellmann, C. Hocke, U. Pietrzyk, M. E. Casey, and T. Kuwert, "NEMA NU2-2001 guided performance evaluation of four Siemens ECAT PET scanners," IEEE Trans. Nucl. Sci. **51**, 2662–2669 (2004).
[5]National Manufacturers Association, NEMA Standards Publication No. NU 2-2001 (National Electrical Manufacturers, Washington, DC, 2001).
[6]National Manufacturers Association, NEMA Standards Publication No. NU 2-2007 (National Electrical Manufacturers, Washington, DC, 2007).
[7]E. J. Hoffman, S. C. Huang, M. E. Phelps, and D. E. Kuhl, "Quantitation in positron emission computed tomography: 4. Effect of accidental coincidences," J. Comput. Assist. Tomogr. **5**, 391–400 (1981).
[8]C. de Boor, *A Practical Guide to Splines* (Springer-Verlag, New York, 1978).
[9]D. Marquardt, "An algorithm for least-squares estimation of nonlinear parameters," SIAM J. Appl. Math. **11**, 431–441 (1963).
[10]C. C. Watson, M. E. Casey, L. Eriksson, T. Mulnix, D. Adams, and B. Bendriem, "NEMA NU 2 performance tests for scanners with intrinsic radioactivity," J. Nucl. Med. **45**, 822–826 (2004).
[11]H. W. de Jong, F. H. van Velden, R. W. Kloet, F. L. Buijs, R. Boellaard, and A. A. Lammertsma, "Performance evaluation of the ECAT HRRT: An LSO-LYSO double layer high resolution, high sensitivity scanner," Phys. Med. Biol. **52**, 1505–1526 (2007).
[12]K. Wienhard *et al.*, "The Ecat exact HR—Performance of a new high-resolution positron scanner," J. Comput. Assist. Tomogr. **18**, 110–118 (1994).
[13]S. Surti and J. S. Karp, "Imaging characteristics of a 3-dimensional GSO whole-body PET camera," J. Nucl. Med. **45**, 1040–1049 (2004).
[14]J. S. Kim *et al.*, "Performance measurement of the microPET Focus 120 scanner," J. Nucl. Med. **48**, 1527–1535 (2007).
[15]National Manufacturers Association, "Performance measurements of small animal positron emission tomographs," NEMA Standards Publication No. NU 2-2008 (National Electrical Manufacturers, Washington, DC, 2008).
[16]Y. C. Tai *et al.*, "Performance evaluation of the microPET Focus: A third-generation microPET scanner dedicated to animal imaging," J. Nucl. Med. **46**, 455–463 (2005).
[17]C. C. Watson, "New, faster, image-based scatter correction for 3D PET," IEEE Trans. Nucl. Sci. **47**, 1587–1594 (2000).
[18]M. Lubberink, S. A. van, H. W. de Jong, G. A. van Dongen, and G. J. Teule, "Acquisition settings for PET of 124I administered simultaneously with therapeutic amounts of 131I," J. Nucl. Med. **47**, 1375–1381 (2006).

Therapeutic efficacy of a polymeric micellar doxorubicin infused by convection-enhanced delivery against intracranial 9L brain tumor models

Tomoo Inoue, Yoji Yamashita, Masamichi Nishihara, Shinichiro Sugiyama, Yukihiko Sonoda, Toshihiro Kumabe, Masayuki Yokoyama, and Teiji Tominaga

Department of Neurosurgery, Tohoku University Graduate School of Medicine, Sendai (T.I., Y.Y., S.S., Y.S., T.K., T.T.), and Yokoyama Nano-medical Polymers Project, Kanagawa Academy of Science and Technology, Kawasaki (M.N., M.Y.); Japan

Convection-enhanced delivery (CED) with various drug carrier systems has recently emerged as a novel chemotherapeutic method to overcome the problems of current chemotherapies against brain tumors. Polymeric micelle systems have exhibited dramatically higher in vivo antitumor activity in systemic administration. This study investigated the effectiveness of CED with polymeric micellar doxorubicin (DOX) in a 9L syngeneic rat model. Distribution, toxicity, and efficacy of free, liposomal, and micellar DOX infused by CED were evaluated. Micellar DOX achieved much wider distribution in brain tumor tissue and surrounding normal brain tissue than free DOX. Tissue toxicity increased at higher doses, but rats treated with micellar DOX showed no abnormal neurological symptoms at any dose tested (0.1–1.0 mg/ml). Micellar DOX infused by CED resulted in prolonged median survival (36 days) compared with free DOX (19.6 days; $p = 0.0173$) and liposomal DOX (16.6 days; $p = 0.0007$) at the same dose (0.2 mg/ml). This study indicates the potential of CED with the polymeric micelle drug carrier system for the treatment of brain tumors. *Neuro-Oncology 11, 151–157, 2009 (Posted to Neuro-Oncology [serial online], Doc. D08-00039, August 28, 2008. URL http://neuro-oncology.dukejournals.org; DOI: 10.1215/15228517-2008-068)*

Keywords: brain tumors, convection-enhanced delivery, doxorubicin, drug delivery system, polymeric micelle

Received February 18, 2008; accepted July 22, 2008.

Address correspondence to Yoji Yamashita, Department of Neurosurgery, Tohoku University Graduate School of Medicine, 1-1, Seiryo-machi, Aoba-ku, Sendai 980-8574, Japan (yoji@nsg.med.tohoku.ac.jp).

Convection-enhanced delivery (CED) is a promising local delivery technique using bulk flow to deliver low-molecular-weight and macromolecular drugs directly to targeted sites in clinically significant volumes of tissue and to achieve wider volumes of distribution compared with simple diffusion techniques.[1] CED bypasses the blood–brain barrier that prevents most anticancer drugs from penetrating into the CNS, delivers a high concentration of therapeutic agents to the targeted site, and minimizes systemic exposure, resulting in fewer side effects.[1] Many antineoplastic drugs,[2–5] including immunotoxins and boronated drugs,[6,7] have been administered using CED, with promising outcomes in animal studies. The problems include rapid drug clearance from the tumor interstitium,[6] no selective accumulation in targeted tissues,[7] and brain damage caused by highly cytotoxic agents with extensive distribution in the CNS.[2–5] Consequently, novel drug delivery systems are necessary to achieve the highest possible therapeutic index against tumor cells over healthy neuronal cells.[8,9]

Incorporation or attachment of low-molecular-weight anticancer drugs into drug carriers with high molecular

weight and hydrophilicity may provide substantial inhibition of drug clearance from the tumor interstitium, in contrast to low-molecular-weight drugs that are cleared very rapidly by active transport via proteins such as P-glycoprotein as well as by passive diffusive transport through the lipid bilayer of the endothelium. The drug carrier systems also offer the advantage of sustained drug release, as prolonged exposure time is more important than the peak concentration factor for many anticancer drugs. However, only liposomes have been studied as drug carriers in combination with CED.[8–12]

Polymeric micelles are an assembly of synthetic polymers, most typically block copolymers with both hydrophobic and hydrophilic blocks. Polymeric micelle carrier systems were first studied for targeting solid tumors by intravenous injection.[13–16] Polymeric micelle carrier systems are electrically neutral and so have the so-called stealth property that evades rapid clearance at the reticuloendothelial systems,[17] which substantially improves targeting of murine solid tumors due to the enhanced permeability and retention effect that depends on the hyperpermeable vasculature and absence of effective lymphatic drainage that prevents efficient clearance of micromolecules in the solid tumor tissues.[18] Polymeric micelles incorporating micellar doxorubicin (DOX) were initially developed to enhance the safety and efficacy of conventional DOX.[13] Various micelle-encapsulated cytotoxic agents are currently undergoing clinical evaluation of systemic administration, including DOX,[9] paclitaxel,[19] cisplatin,[20] camptothecin,[21] and the camptothecin derivative SN-38.[22] In contrast, local delivery of polymeric micelle systems for the treatment of brain tumors remains relatively unexplored.

The present study evaluated the therapeutic possibilities of micellar DOX in a 9L syngeneic rat brain tumor model.

Materials and Methods

Preparation of Agents

Doxorubicin hydrochloride was purchased from Mercian Corp. (Tokyo, Japan). Stock solutions of free DOX were prepared by diluting DOX in dimethyl sulfoxide to a concentration of 50 mg/ml. The infusion solution of free DOX was made by diluting the stock solution with phosphate-buffered saline (PBS). Liposomal DOX (Doxil) was obtained from Alza Pharmaceuticals (Mountain View, CA, USA). Micellar DOX was prepared by the previously reported method in a slight modification only in high-performance liquid chromatography (HPLC) analysis conditions.[14–16] In brief, DOX was chemically conjugated to the aspartic acid residue of poly(ethylene glycol)-b-poly(aspartic acid) block copolymer. The hydrophobicity of the DOX-conjugated poly(aspartic acid) block results in the formation of a polymeric micelle structure. This conjugate block copolymer was used to form empty polymeric micelles in this study because this type of micelle does not contain unbound DOX that is important in cytotoxic activity. Free DOX was incorporated into empty polymeric micelles to form pharmacologically active polymeric micelles that contain free DOX in the micelle inner core. The poly(ethylene glycol) block had a molecular weight of 12 kDa and contained 22 aspartic acid units as determined by ^{1}H-nuclear magnetic resonance spectrum in D_2O. DOX was chemically conjugated to 59% of the aspartic acid residues, and the micelles contained 13 wt% free DOX. The amounts of the chemically conjugated DOX and the physically entrapped DOX were determined by a reverse-phase HPLC according to methods previously reported.[15,16] The empty polymeric micelles (DOX was not physically entrapped) chemically conjugated DOX molecules to 68% of the aspartic acid residues. The infusion solution for micellar DOX, PBS, had no toxicity when 20 µl was infused by CED (preliminary data not shown).

Tumor Cell Lines

9L gliosarcoma cells (American Type Culture Collection, Rockville, MD, USA) were maintained as monolayers in a complete medium consisting of Eagle's minimal essential medium supplemented with 10% fetal calf serum, nonessential amino acids, and 100 U/ml penicillin G. Cells were cultured at 37°C in a humidified atmosphere consisting of 95% air and 5% CO_2.

Animals and Intracranial Syngeneic Transplantation Technique

All protocols utilized in the animal studies were approved by the Institute for Animal Experimentation of Tohoku University Graduate School of Medicine. Male Fischer 344 rats weighing 150–200 g and normal male Sprague-Dawley rats weighing approximately 150–200 g were purchased from Charles-River Laboratories (Charles-River Japan Inc., Tsukuba, Japan). For the intracranial syngeneic tumor model, 9L gliosarcoma cells were harvested by trypsinization, washed once with Hanks' balanced salt solution without Ca^{2+} and Mg^{2+} (HBSS), and resuspended in HBSS for implantation. Cells (5×10^5) in 10 µl HBSS were implanted into the striatal region of the rat brains as follows. The rats under deep isoflurane anesthesia were placed in a small-animal stereotactic frame (David Kopf Instruments, Tujunga, CA, USA). A sagittal incision was made to expose the cranium, followed by a burr hole in the skull at 0.5 mm anterior and 3 mm lateral from the bregma using a small dental drill. Cell suspension (5 µl) was injected over 2 min at a depth of 4.5 mm from the brain surface; after a 2-min wait, another 5 µl was injected over 2 min at a depth of 4.0 mm, and after a final 2-min wait, the needle was removed and the wound was sutured.

CED Infusion

CED of PBS, free DOX, liposomal DOX, and micellar DOX was performed as described previously.[9,11] The infusion system consisted of a reflux-free step design infusion cannula[23] connected to a loading line (containing 20 µl PBS, free DOX, liposomal DOX, or micellar

DOX solutions) and an olive oil infusion line. A 1-ml syringe (filled with oil) was mounted onto a microinfusion pump (BeeHive; Bioanalytical Systems, West Lafayette, IN, USA) to regulate the flow of fluid through the system. Based on chosen coordinates, the infusion cannula was mounted onto a stereotactic holder and guided to the target region of the brain through burr holes made in the skull (see below). The infusion rates followed the following ascending pattern to deliver the total 20-µl infusion volume: 0.2 µl/min (15 min) + 0.5 µl/min (10 min) + 0.8 µl/min (15 min).

Evaluation of Distribution of Micellar DOX in Normal Rodent CNS

Normal Sprague-Dawley rats (five rats in each group) received CED using free DOX (2 mg/ml DOX in 20 µl solution), liposomal DOX (20 µl solution containing 2 mg/ml DOX equivalent), and micellar DOX (20 µl solution containing 2 mg/ml physically entrapped DOX and 4.3 mg/ml chemically conjugated DOX equivalent), and empty polymeric micelles (20 µl solution containing 7.9 mg/ml chemically conjugated DOX equivalent) and were euthanized immediately after CED. The brains were harvested, frozen in isopentane chilled in dry ice, and cut into serial coronal sections (25 µm) with a cryostat. DOX fluoresces under UV illumination, so the areas of distribution could be visualized by fluorescence microscopy and captured with a charged-coupled device camera with a fixed aperture. The empty polymeric micelles were also fluorescent in a similar manner to the micellar DOX, since the empty polymeric micelles contained chemically conjugated DOX molecules that were almost equivalent in their fluorescent behavior to physically entrapped DOX of the micellar DOX. The volume of distribution was analyzed with a Macintosh-based image-analysis system (NIH Image 1.62; NIH, Bethesda, MD, USA) as described previously.[24]

Evaluation of Distribution of Micellar DOX in Rats with 9L Intracranial Tumors

Fischer 344 rats (four rats in each group) with 9L intracranial tumors received CED using micellar DOX and free DOX (20 µl solution containing 2 mg/ml DOX equivalent) 7 days after tumor cell implantation. Rats were euthanized immediately after CED. The brains were harvested, frozen in isopentane chilled in dry ice, and cut into serial coronal sections (25 µm) with a cryostat.

Toxicity Tests of Micellar DOX

Normal Sprague-Dawley rats (five rats in each group) received a single CED infusion of free DOX, liposomal DOX, micellar DOX, and empty polymeric micelles (20 µl solutions containing 0.1, 0.2, 0.4, or 1.0 mg/ml free DOX equivalent). Rats were monitored daily for survival and general health (alertness, grooming, feeding, excreta, skin, fur, mucous membrane conditions, ambulation, breathing, and posture) and weekly for weight. The rats in each group were euthanized 3 weeks after the CED treatment, and their brains were removed, fixed, cut into sections (5 µm), and stained with hematoxylin and eosin (H&E).

Survival Studies

Fifty-two Fischer 344 rats with 9L tumor cells were randomly assigned to four groups: (1) the control group that received PBS (20 µl solution; $n = 17$), (2) free DOX (0.2 mg/ml DOX in 20 µl solution; $n = 10$), (3) liposomal DOX (20 µl solution containing 0.2 mg/ml DOX equivalent; $n = 14$), and (4) micellar DOX (20 µl solution containing 0.2 mg/ml physically entrapped free DOX equivalent; $n = 11$). Seven days after tumor cell implantation, a single CED infusion was performed for each group. Rats were monitored daily for survival and general health, and weekly for weight. The study was terminated 90 days after tumor implantation. The surviving animals were euthanized and their brains stained with H&E. Survival was expressed as a Kaplan-Meier curve. Survival between the treatment groups was compared with a log-rank test.

Results

Evaluation of Distribution of Micellar DOX in Normal Rodent CNS

Compared with free DOX (Fig. 1a), intrastriatal administration of liposomal DOX (Fig. 1b), micellar DOX (Fig. 1c), and empty polymeric micelles (Fig. 1d) via CED (20 µl volume) produced extensive and diffuse distribution in the striatum. The mean volumes of distribution of free DOX, liposomal DOX, micellar DOX, and empty polymeric micelles in normal rat brains were 13.91 ± 1.23 mm^3 (range, 12.12–15.32 mm^3), 64.25 ± 7.83 mm^3 (54.76–77.40 mm^3), 60.54 ± 5.71 mm^3 (54.40–64.25 mm^3), and 54.74 ± 4.39 mm^3 (50.30–58.97 mm^3), respectively (Fig. 1e). A significant difference was observed between free DOX and micellar DOX ($p = 0.009$), but not between liposomal DOX and micellar DOX ($p = 0.465$).

Evaluation of Distribution of Micellar DOX in Rats with 9L Tumors

Examination of representative rat brain sections at 1-mm intervals confirmed successful formation of the tumor tissue. Fluorescent detection of DOX in the same sections revealed poor distribution of free DOX (Fig. 2a) but distribution of micellar DOX over almost the entire tumor mass, including the surrounding tumor margins (Fig. 2b). The findings were consistent in all four rats examined from this group.

Toxicity of Micellar DOX in Normal Rodent CNS

Rats euthanized 3 weeks after infusion with 0.2 (Fig. 3a, center), 0.4 (Fig. 3a, right), and 1.0 (data not shown) mg/ml micellar DOX showed tissue damage at the infusion